Super-resolving particle diffusion heterogeneity in porous hydrogels via high-speed 3D active-feedback single-particle tracking microscopy

Authors: Yuxin Lin[1], Haoting Lin[1], Kevin D. Welsher[1]*

[1]Department of Chemistry, Duke University; Durham, North Carolina 27708, United States

*Corresponding author. Email: kdw32@duke.edu

ABSTRACT: Nanoparticle diffusion in 3D porous structures is critical to understanding natural and synthetic systems but remains underexplored due to limitations in traditional microscopy methods. Here, we use 3D Single-Molecule Active-feedback Real-time Tracking (3D-SMART) microscopy to resolve nanoparticle dynamics in agarose gels with unprecedented spatiotemporal resolution. We highlight 'hopping diffusion', where particles intermittently escape confinement pockets, providing insights into hydrogel microstructure. Long, highly sampled trajectories enable extraction of kinetic parameters, confinement sizes, and thermodynamic barriers. This study demonstrates 3D-SMART's ability to probe particle-environment interactions at super-resolution (~10 nm in XY and ~30 nm in Z) in 3D, offering new perspectives on nanoparticle diffusion and the structural dynamics of porous materials, with implications for drug delivery, material science, and biological systems.

INTRODUCTION

In recent years, the development and application of single-particle tracking across many fields has been widespread.[1-4] However, nanoparticle (NP) diffusion and interaction within 3D structures remain underexplored. Nanoparticle diffusion within porous microstructures is scientifically intriguing and crucial in both natural and synthetic systems. Porous microstructures dramatically

impact the diffusion and penetration of nanoparticles. For example, mucus clearance acts as a primary barrier against viral infection and serves as an obstacle to be overcome for intranasal drug delivery.[5, 6] In gel electrophoresis and column chromatography, the diffusion of nanoparticles within complex 3D environments may provide critical structural characterization.[7]

Electron and force microscopies are common tools for studying the structure and mechanical properties of hydrogels and other microporous structures. Unfortunately, both typically involve perturbative experimental requirements that irreversibly alter the microstructures and cannot resolve particle dynamics within the hydrogel.[8, 9] Single-particle tracking (SPT) microscopy, or microrheology, is a frequent tool for studying the interaction of nanoparticles and microstructures.[10] Trajectories of single particles are usually achieved using image-based methods, in which the particle of interest is imaged sequentially, and localizations are concatenated into a trajectory.[2, 11] However, limitations exist for image-based tracking methods in terms of observation duration, lack of spatiotemporal resolution, and restriction to two-dimensional motion.[12-14] When particle motion is confined to two-dimensions (and just one focal plane), the temporal resolution is limited by the time it takes to collect one image, determine by the number of pixels and pixel dwell time for confocal methods, and camera exposure and readout for widefield methods. However, for three-dimensional processes, the particle localization rate is limited by the volumetric imaging rate, which is the single focal plane imaging rate multiplied by the number of planes required, dramatically decreasing the temporal resolution. One approach to break this volumetric imaging bottleneck is to apply point spread function (PSF) engineering to encode axial information into the 2D image of a single particle. However, most reported PSF engineering approaches are restricted to an axial range of a few microns,[15] which is still not ideal for thicker hydrogels. The scattering induced by the thick and complex 3D matrix will also pose a further challenge to PSF engineering methods. An alternative approach called fcsSOFI,[7, 16] developed by Kisley *et al*, combines super-resolution optical fluctuation imaging (SOFI) and fluorescence correlation spectroscopy (FCS) and is a powerful tool to characterize spatial and diffusion information within porous materials. fcsSOFI overcomes the problem with limited sampling in SPT but sacrifices dynamic information that can be extracted from single particle trajectories. Also, in most applications of the methods mentioned above, single-particle trajectories are very challenging to understand due to high noise and short observation time, diminishing the potential to understand the behaviors of individual particles in detail. Short, noisy, and low sampling rate

trajectories limit the knowledge that can be extracted. Often, the best that can be expected is the measurement of a diffusion coefficient or extraction of non-Brownian behavior from an ensemble mean-square displacement (MSD) analysis. Long, highly sampled, three-dimensional trajectories are needed to extract the structure and dynamics of porous materials. In this work, we demonstrate that active-feedback 3D single-particle tracking microscopy is well-suited for super-resolving gel structure and dynamics in three dimensions.

Recent years have seen a wide range of applications of active-feedback tracking microscopy.[3, 17-23] Active-feedback microscopy presents a unique opportunity to demystify hydrogel microstructures along larger spatial, especially axial, scales with greater detail. Instead of taking images sequentially, active-feedback tracking microscopy uses modified detection[24] or patterned excitation[25, 26] to obtain real-time localization information of rapidly diffusing particles and uses a closed feedback loop to "lock" the particle in the center of the observation volume. Active-feedback tracking microscopy uses previous particle position and updated photon information for real-time location estimation; thus, by using information from prior localizations, fewer photons are required for better spatial and temporal resolution compared to image-based methods. Also, the typical excitation or detection module is three-dimensional. It is not required to take images at multiple planes and assemble them into a stack (z-stacking) for tracking along the axial direction, which greatly enhances the sampling rate for 3D tracking.

Here, we used 3D Single-Molecule Active-feedback Real-time Tracking (3D-SMART) microscopy to monitor the three-dimensional dynamics of nanoparticles within agarose gels (AG) with high spatiotemporal resolution and long tracking duration. Notably, in larger nanoparticles and higher concentration AG preparations, it is frequently observed that particles can repeatedly "hop" between confinement cages or explore the interior of hydrogel in a hopping diffusion manner. Kinetic parameters, such as the lifetimes, on/off rates, and hopping energy barriers can be extracted from highly sampled trajectories. The highly sampled trajectories depicted the complex 3D environment and could be utilized to probe the microstructures with super-resolution of ~ 10 nm.

RESULTS

High spatiotemporal SPT via 3D-SMART

Agarose gels (AG) were chosen as the model system for this work due to their extensive use in biomolecule separations and thorough characterization.[27] Fluorescent nanoparticles of different sizes were premixed within agarose gels of desired concentrations. High-speed single-particle tracking was accomplished by 3D-SMART microscopy as previously described (Fig. 1, fig. S1).[25, 28, 29] Briefly, a 3D scanning volume of 1 × 1 × 2 μm in XYZ was generated laterally with a pair of electric-optical deflectors (EODs, ConOptics, M310A) and axially with a tunable acoustic gradient (TAG, TAG Optics, TAG 2.0) lens.[30] The lateral plan is a 5 × 5 grid sampled at 20 μsec per spot, while the focus is simultaneously scanned at 70 kHZ in Z. The photon arrival information was captured by a single photon counting avalanche photodiode (APD, Excelitas, SPCM-ARQH-25) and applied to estimate the real-time position of the particle with an assumed Gaussian density Kalman filter.[31] The real-time position estimation was used to drive the piezoelectric stage to 'lock' the diffusing particle in the center of the scanning volume.

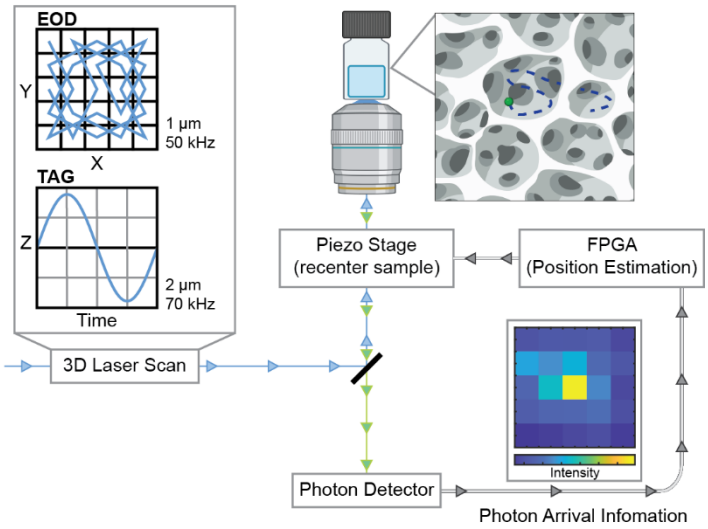

Figure 1. Illustration of performing SPT in hydrogels using 3D-SMART. A sub-millisecond 3D scanning volume of 1×1×2 μm is generated by a pair of EODs and a TAG lens. Probes were premixed with the desired concentration of agarose gel solution and solidified in the chamber. The photon detector (APD) collects the emitted photons, and photon arrival information is routed into an FPGA for real-time position estimation of the diffusing probe. The updated localization information is used to drive the piezoelectric stage to effectively hold the diffusing nanoparticle in the center of the laser scan.

The position sampling rate of 3D-SMART is 1 kHz, corresponding to the piezoelectric stage's response time. The lateral localization precisions are about 10 nm with 300 kHz intensity (i.e., 300 photons in 1 ms bin time, fig. S2a-b). Compared to non-gel tracking, the axial tracking localization

precision (29.7 ± 2.8 nm) in AG was slightly reduced due to scattering in the gel network (fig. S2c). In addition to the 1 kHz position sampling of 3D-SMART, the photon arrivals can be assembled into an image called the "EOD Image." The EOD image is a critical piece of information that allows confirmation that trajectories arise from a single particle (fig. S8, also see Methods section for more details).

Particle diffusion is hindered by concentrated hydrogel and large particle size

First, passive diffusion of fluorescent nanoparticles of various sizes within the agarose gel of different concentrations was observed (see Methods). The results and tendencies were very intuitive and similar to expected and previously reported results.[32] For probes of the same size, the degree of spatial confinement increased with increasing agarose concentration, leading to more hindrance of the particle diffusion (Fig. 2A). While for the same agarose gel, the larger beads tend to be more confined while smaller beads diffuse freely (Fig. 2C). Trajectories were quantified using diffusion coefficient (D), power exponent α, and packing coefficient (Pc). A power-law mean-square displacement (MSD) analysis is typically applied for anomalous diffusion.

$$MSD(\tau) = 2nD\tau^{\alpha} \tag{1}$$

Where n is the number of dimensions, D is the diffusion coefficient, τ is the lag time, and the exponent α is used to classify anomalous diffusion ($\alpha < 1$: subdiffusion; $\alpha = 1$: Brownian motion; $\alpha > 1$: superdiffusion).

However, in practice, MSD has limitations when exploring highly confined trajectories. While α can be used to characterize sub-diffusion, experimental values for α exhibit a wide and noisy distribution for highly diffusive particles. On the other extreme, for groups with lower diffusivities, α varies little and is not very informative (fig. S5). An alternative method to quantify lateral subdiffusion is the packing coefficient (Pc), which was demonstrated by Triller et al. to be a powerful tool in distinguishing confinements.[33] It compares the lateral displacements in a time window and the occupied surface area:

$$Pc_i = \sum_{i}^{i+n-1} \frac{(x_{i+1} - x_i)^2 + (y_{i+1} - y_i)^2}{S_i^2} \tag{2}$$

where x_i, y_i are the coordinates at time i; n is the length of the time window; and S_i is the surface area of the convex hull of the trajectory segment between time points i and $i + n$. A

larger packing coefficient means a higher degree of confinement. A window of n = 1000 time points (1 second) was used throughout the analysis unless otherwise indicated.

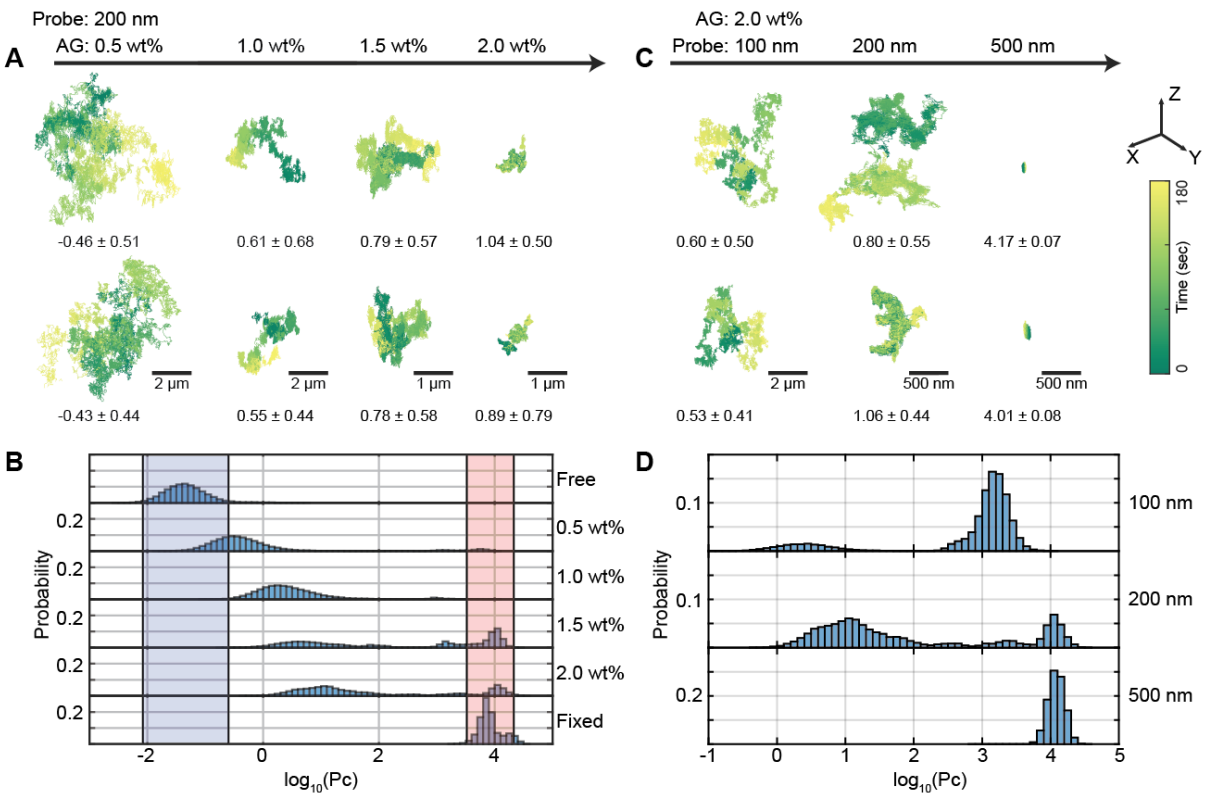

Figure 2. Meshsize- and probe-size dependent diffusion. (**A**) Representative trajectories of 200 nm probes diffusing in increasing wt% AG (see detailed information in fig. S3. N = 51 and 31 for control groups of free and fixed respectively. N = 59, 52, 127, and 93 for 0.5, 1.0, 1.5 and 2.0 wt% AG, respectively). Scale bars: 0.5 wt% and 1.0 wt%: 2 μm; 1.5 wt% and 2.0 wt%: 1 μm. All trajectories in (**A**) and (**C**) share the same colorbar and axis. (**B**) Distribution of packing coefficients of 200 nm probes diffusing in water, increasing wt% AG, and fixed on the surface of the coverslip, respectively. The range of *Pc* is highlighted in red for fixed 200 nm probes (mean ± 2×std) and purple for freely diffusing 200 nm probes (mean ± 2×std). (**C**) Representative trajectories of probes of different sizes diffusing within 2.0 wt% AG (see detailed information in fig. S4. N = 141, 127, and 57 for 100, 200, and 500 nm probes, respectively). Scale bars: 100 nm probes: 2 μm; 200 nm and 500 nm probes: 500 nm. (**D**) Distribution of packing coefficients of different-sized probes diffusing in 2.0 wt% AG.

Packing coefficient analysis showed a clear increasing trend of confinement with increasing concentration of AG and probe size (Fig. 2B and D), in agreement with prior reports that higher agarose concentrations result in smaller pore sizes in the gel.[27] Presumably, as the particle size approaches the pore size, particles exhibit more confined diffusion. In some cases, probes dwelled in or repeatedly visited the same confinement pore. For 200 nm probes, when the AG concentration

reached 1.0 wt%, hopping diffusion started to be observed: particles underwent confined diffusion in one area and intermittently escaped to neighboring areas through connective channels. Hopping escapes between two confinements always featured larger displacement and were highly one-dimensional, in contrast to confined diffusion (fig. S6). Various diffusive behaviors were observed after hopping events. Some particles hopped to relatively free diffusion (see examples in fig. S3b), while others hopped to a neighboring pore and exhibited confined diffusion (see examples in fig. S3c-d). With the combination of larger particles and denser AG, e.g., 2 wt% AG and 200 nm probes, hopping diffusion became a major diffusion pattern for particles to explore the porous hydrogel passively.

Due to the 3D nature of hydrogels, the ability to resolve diffusion and confinement structures in 3D is critical. In active feedback tracking microscopy, particles can be tracked across an ample axial range without sacrificing spatial or temporal resolution. An example of 3D pore-to-pore hopping diffusion is depicted in Fig. 4A-B (see also movie S1), in which the particle hopped through four major cavities in a nonconsecutive manner. After being trapped in the first pore for ~ 25 seconds, the particle bypassed two cavities briefly and thoroughly explored the fourth cavity first. However, the particle swung back eventually, further sampling the second and third previously ignored confinements. Another example trajectory (Fig. 4C, see also Movie S2) shows that hopping diffusion also occurs across a wide axial range, posing challenges to conventional tracking methods to capture and resolve. The ability to track and resolve 3D spatial information is critical when tracking smaller probes in looser meshes due to increased diffusivity.

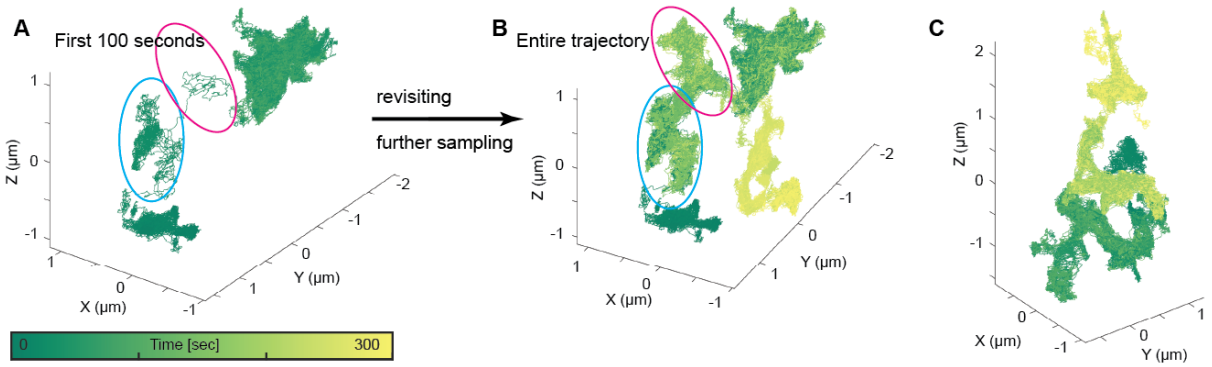

Figure 3. Examples of 3D pore-to-pore hopping diffusion. (**A** and **B**) the first 100-second segment and the entire trajectory of a 200 nm probe diffusing within 2 wt% AG. The red and blue circles highlight two cavities were initially bypassed but eventually revisited after multiple hopping events. (**C**) Another example of a 200 nm probe

diffusing within 2 wt% AG covering a relatively large 3D volume. The same colorabar from (A) applies to all three plots.

Thermodynamics of hopping diffusion

The high sampling rate and precise localization of 3D-SMART enabled analysis of the thermodynamics of hopping diffusion in AG beyond what is possible with traditional SPT. Extraction of the 3D nanoscale structure is required to determine the underlying thermodynamic within heterogeneous and porous materials. To that end, confinement pockets of diffusing particles were identified and segmented based on the dwell time in each pixel (2D) or voxel (3D) (see Methods for details). For example, as shown in Fig. 4, a 180-second 3D trajectory of a 200 nm probe diffusing within 2.0 wt% AG (Fig. 4A) was binned into 10×10×20 nm voxels (XYZ, determined by 3D localization precision). This 3D binned data was then converted into a 3D heatmap representing the dwell time within each voxel. The 3D hotspots in the heatmap correspond to the confinement pockets where the particle repeatedly visited and dwelled. Based on the intensity of the heatmap, the voxels were grouped, allowing the identification of four distinct confinements of different shapes and sizes (Fig. 4B). The volume of the confinement was then calculated from the number of voxels, while the dwell time for each confinement was calculated from the number of localizations within a confinement.

To better understand the thermodynamics of hopping diffusion, we analyzed the relationship between fractional dwell time and fractional confinement volume. Fractional dwell time was calculated as the dwell time in each confinement divided by the total dwell time across all confinements within the trajectory. Fractional confinement volume was similarly defined as the volume of each confinement divided by the total volume of all confinements. Three experimental setups were analyzed: 200 nm probes in 1.5 wt% AG, 200 nm probes in 2.0 wt% AG, and 100 nm probes in 2.0 wt% AG. In all cases, a clear one-to-one relationship between fractional dwell time and confinement volume was observed, indicating that hopping diffusion is governed purely by entropic differences between the pores (see Methods for details), which is determined by pore size. Furthermore, this relationship suggests that the free energy difference, ΔF, between two adjacent confinements is proportional to the ratio of their confinement volumes:

$$\Delta F = -k_B T \ln\left(\frac{V_2}{V_1}\right) \tag{3}$$

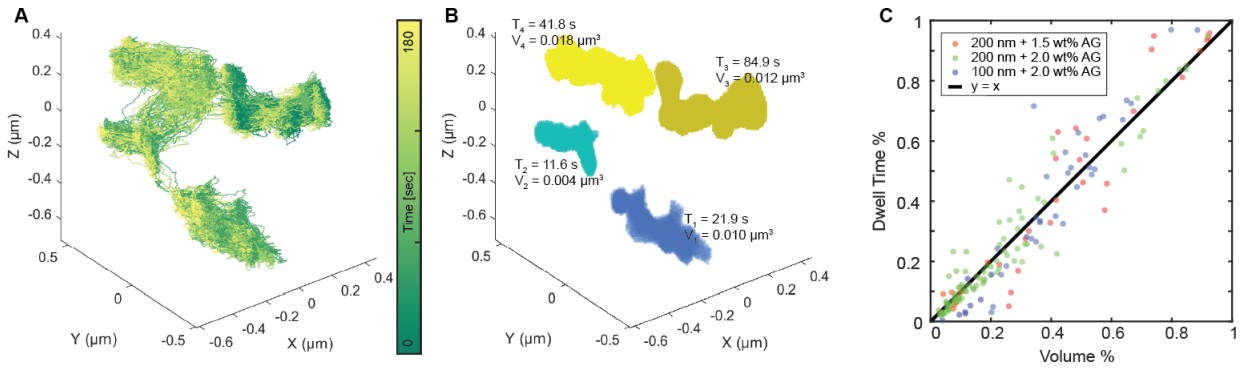

Figure 4. (**A**) 3D trajectory of 200 nm probe's hopping diffusion within 2.0 wt% AG. Trajectory is color-coded by time. (**B**) Four identified confinements of the trajectory shown in (**A**), with corresponding dwell time (T) and confinement volume size (V). The color code represents the number of confinement. (**C**) Plot of the fractional volume against the fractional dwell time, indicating hopping diffusion is driven by entropic differences between confinement areas.

Kinetic information extracted from hopping events

Multiple factors, including the particle diameter, size of the channel, and length of agarose polymers occupying the channel, may determine the free energy barrier the particle needs to hop from one pore to another.[34, 35] The heterogeneous nature of the agarose gel makes it challenging to probe the energy barrier from hopping diffusion in typical single-particle trajectories. Trajectories collected by 3D-SMART have the advantage of having high spatiotemporal precision, enabling frequently sampled and precise trajectories that can map out the entire environment of the particle, given a suitable duration of observation. Using 3D-SMART, it was observed that particles could hop between two adjacent pores repeatedly, allowing for a thorough sampling of the channel between the pores (Fig. 5A-B, see also Movie. S3). From these trajectories, it is possible to gain a detailed understanding of the geometry of both the pores and the connecting channels and enable a detailed analysis of the kinetics of hopping diffusion.

To better analyze these hopping events, the confinement pockets of each 3D trajectory were identified using the algorithm mentioned above in both 2D and 3D. A 2D heatmap (density of the probe centroid localizations) is shown in Fig. 5D and also serves as an indirect visualization of the interior microstructures carved out by the particle trajectory. Transitional localizations between two cavities were specifically extracted to measure the width of the "channel" connecting two

pores and to measure the kinetics and thermodynamics of hopping events through these channels. The channel shown in Fig. 5d is very narrow and only 68.0 ± 3.3 nm (Calculated as 3 × std representing ~86% of the datapoints, Fig. 5G) wider than the probe. Based on the intensity on the heatmap, the localizations of two states can be labeled accordingly as pores 1 and 2, with volumes of 0.012 ± 0.0010 and 0.009 ± 0.0008 μm^3 (2D area size: 0.092 ± 0.0002 μm^2 and 0.048 ± 0.0001 μm^2, respectively (Fig. 5E). Although their trajectories appeared relatively unremarkable along the axial dimension, the projected 2D area sizes of each confinement were 0.092 μm^2 and 0.048 μm^2, with a ratio of 1.9 (compared to the volume ratio of 1.3). This discrepancy may lead to an inaccurate estimation of the thermodynamic barrier. The translocation rate between the two confinements was also calculated as the inverse of lifetimes in each confinement (Fig. 5F, fig. S10), which were 0.231 ± 0.050 and 0.227 ± 0.048 s^{-1}, respectively.

MSD analysis (2D MSD: Fig. 5C; 3D MSD: fig. S14) reveals several different diffusion states for hop events. The particle first explored the cavities freely with exponent $\alpha \approx 1$ for the first ~ 40 ms. After this free diffusion regime, the particle motion became subdiffusive with the MSD proportional to the square root of lag time up until ~3 sec. After the probe thoroughly explored the pores, the MSD fluctuates around a maximum value 0.18 ± 0.02 μm^2 (calculated based on MSD value after 3.2 sec), corresponding to a gyration diameter of 0.85 μm (0.94 μm for 3D). This gyration diameter provides a rough estimate of the area explored by the entire trajectory but may be less informative for irregularly shaped trajectories like the one presented here. Indeed, this value does roughly agree with the combined gyration diameters of the individual pores, which were ~1.02 μm in 2D or ~0.88 μm in 3D, respectively.

Hop events between pores are very short duration (~ 6 ms, fig. S6a), highly one-dimensional along the channel (fig. S6b-c), and show slightly larger displacements (13 [8, 18] nm in pores, 19 [13, 27] nm channel, Median [Q1, Q3], Kruskal-Wallis Test, $p < 0.001$, fig. S6d). We further compared the displacement of unsuccessful hops, in which particles entered the channel but failed to pass through. These unsuccessful hops exhibited smaller displacements (11 [7, 16] nm, median [Q1, Q3], Kruskal-Wallis Test, $p < 0.05$) compared to diffusion in the pores (fig. S6d). As mentioned above, the particle needs to overcome an entropic barrier to pass through the channel. The longer length of successful hops is consistent with a free energy barrier within the channel, while shorter displacements do not have sufficient free energy to overcome the barrier within the channel.

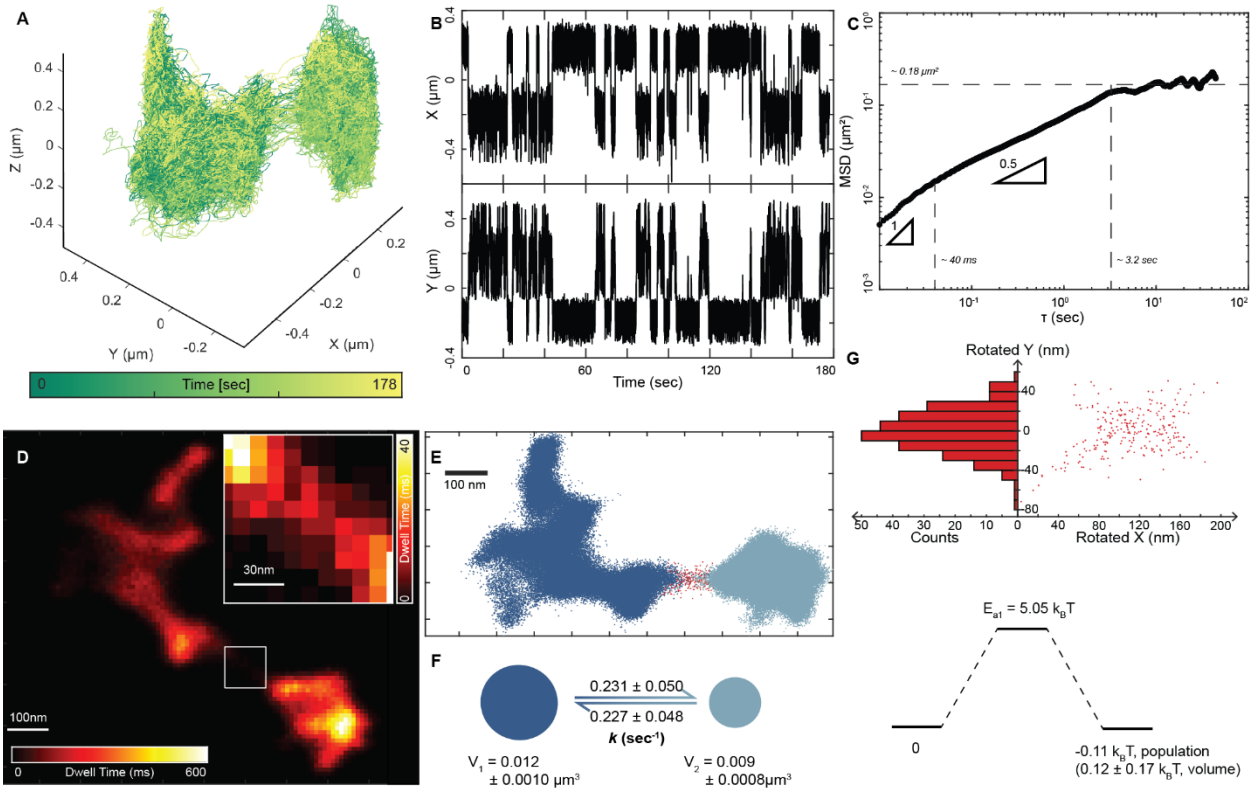

Figure 5. Illustration of a hop event. (**A**) Representative trajectory of hopping events between two cavities. NP size d = 200 nm, AG concentration c = 1.5 wt%. (**B**) X and Y traces of the trajectory shown in (**A**), indicating there existed two states for particle diffusion. (**C**) 2D MSD plot of the representative trajectory shows different diffusive states in cavities connected by a channel (minimum lag time of 10 ms). The two slopes were calculated based on a linear fit within the corresponding time window. Lag times shorter than 10 ms were chopped. see 3D MSD plot in fig. S14. (**D**) 2D heatmap converted from 3D trajectory based on the number of localizations (or dwell time) within each pixel (10×10 nm). Inset: a zoomed-in view of the channel connecting two cavities. (**E**) Rotated view of point cloud of localizations. Dark blue points and light blue points represent two populations, and red points represent the transition between two states. (**F**) Translocation rates, volumes, and areas of two confinements. (**G**) Right: rotated coordinates of the transition points. Left: histogram of the rotated Y position of the transition points as a measurement of the channel width, calculated to be 3 × std = 68.0 ± 3.3 nm (calculated value ± measuring uncertainty). (**H**) Energy diagram of the energy barrier between two confinements and the activation energy of the hop.

The free energy difference between two confinements, ΔF, and the activation energy of hop events, E_a, may be calculated based on the population within the cavities via the Boltzmann distribution:

$$\Delta F = -k_B T \ln(\frac{N_2}{N_1}) \quad (4)$$

$$E_{a1} = -k_B T \ln(\frac{N_{Ch}}{N_1}) \quad (5)$$

where N_1 and N_2 are the population of the two cavities, and N_{Ch} is the population of the channel. The calculated activation energy to hop from pore 1 was 5.05 k_BT, and the free energy difference between the two larger pores was -0.11 k_BT (Fig. 5H). The free energy difference between the pores was also calculated based on the volumetric ratio using Eq. 3, which gave a similar result (+0.12 ± 0.17 k_BT, Fig. 5H). The relatively small energy barrier between the two confinements explains the similar translocation rate between the two cavities. It is worth emphasizing that hop events occur rapidly (~6 ms), and cannot be observed by existing SPT microrheology methods. The population of trajectory points and the energy barrier for hopping diffusion can only be measured by methods with high spatiotemporal precision.

The activation energy and kinetic rates can be further used to interpret the frequency of attempts using the Arrhenius equation:

$$k = Ae^{-\frac{E_a}{k_B T}} \quad (6)$$

in which the frequency factor A corresponds to the frequency of attempts to cross the channel. The frequency factors for transitions from pore 1 to 2 (A_1) and from 2 to 1 (A_2) are identical at 1.17 s^{-1}. Given the 1 kHz sampling rate of the trajectories, this can be translated to 0.117 % of trajectory localizations within each confinement that can be considered attempts at crossing the narrow channel. This attempt frequency can be translated to a distance from the opening of the channel. To determine the distance from the channel that a particle must be to attempt a hop, we examined the cumulative probability of observing a trajectory point as a function of distance from the channel (Fig. 6A). It can be found that the distance at which the cumulative probability reaches 0.117% occurs at 15 nm from the channel for pore 1, and 18 nm from the channel for pore 2, noticeably close to the step size of diffusion within the confinement (13 [8, 18] nm, median [Q1, Q3]). The difference between these attempt distances may reflect difference channel geometries on either side.

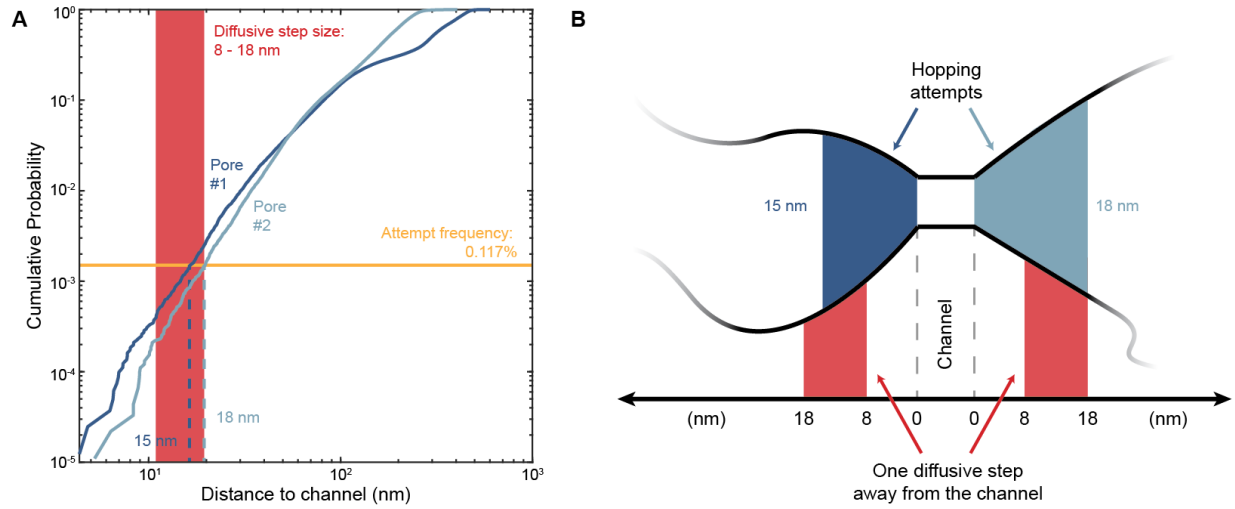

Figure 6. (**A**) Cumulative distribution function (CDF) of particle localizations as a function of distance to the channel for pore 1 and 2. The solid yellow line indicates the 0.117% cumulative probability corresponding to the frequency factor of 1.17 s^{-1} with 1 kHz sampling. The corresponding distance for hopping attempts is 15 nm and 18 nm for confinement 1 and 2, respectively, as noted by the blue lines. (**B**) Illustration showing hopping starts to attempt roughly one diffusive step away from the channel.

Other works have observed diffusion similar to what is captured via 3D-SMART in this work. Two other similar diffusion patterns previously reported were "hopping diffusion"[34, 36, 37] and "diffusive escape."[35] Prior work on hopping diffusion within gel networks describes the fluctuation of a gate between two neighboring confinements, which could allow a particle with size exceeding the network mesh size to hop into a neighboring confinement. In this case, the channel represents the polymer chain fluctuation of the gate, while its volume represents the number of microstates. Based on this hopping diffusion model, the activation energy barrier is given by

$$E_a = k_B T (d/a_x)^2 \tag{7}$$

where d is the particle size, and a_x is the length of the polymer network. Applying this equation to our result in Fig. 5H, we can calculate the length of the polymer network is ~89 nm. While this network length size is within an order of magnitude of the expected size (50 nm to >200 nm for 120 kDa agarose),[38, 39] the network size can be highly affected by entanglement and physical crosslinking, especially in the highly heterogenous agarose gel.

"Diffusive escape" describes Brownian particle escape from confinement through a nanochannel and is usually probed with specially synthesized films, such as a liquid-filled inverse opal film.[35, 40] In the diffusive escape model, the narrow channel itself effectively acts as a free energy barrier,

owing to its limited size, as well as additional repulsive potentials that may prevent translocation through the channel. From the current data, if one assumes that the channel exists physically and is rigid, it is possible to estimate the channel volume based on the localization within the channel by $V \simeq 2\mathrm{std}(x) \times 2\mathrm{std}(y) \times 2\mathrm{std}(z)$ (± 1 σ, containing ~ 68% of the data), which gives a result of 5.28×10^5 nm^3. Plugging that the volume size of pore 1 (0.012 ± 0.0010 μm^3 calculated above) into Eq. 3 yields an estimated activation barrier of 3.20 ± 0.09 k_BT, which is significantly lower than the value of 5.05 k_BT obtained above from localizations within the channel. The discrepancy between these two values indicates that an additional energy barrier exists, in addition to the entropic barrier from the limited channel size. This suggests the presence of additional repulsions that hinder translocation beyond the effect of geometry. Notably, this extra barrier appears to be specific to narrow channels, as larger pores exhibit energy differences dependent solely on their volume. This additional obstacle could stem from the hopping diffusion model discussed above, where polymer chain rearrangement introduces an additional energy barrier. Another possible factor is the electrostatic repulsion between negatively charged particles and the negatively charged gel microenvironment, which would be most pronounced at the interface between channel and pores.

CONCLUSION

In this work, we have demonstrated that active-feedback single-particle tracking methods have great potential for microrheology studies, providing highly spatiotemporally resolved 3D information. The combined high sampling rate, 3D localization, and long duration of observation allowed for the complete characterization of nanoscale confinements and channels within heterogeneous agarose gel networks. The kinetics and thermodynamics of hopping diffusion through nanoscale channels were analyzed from single-particle trajectories. The direct observation of these hopping events between two adjacent nanoscale pores presents a unique opportunity to understand narrow escape events in hydrogel networks. The high spatiotemporal resolution of each single-particle trajectory also enables detailed tracing of the interior microstructure of 3D porous materials (Fig. 3D). While agarose is a highly heterogenous system, the experiments presented here are a good starting point to understand hopping diffusion in more controlled polymer networks and synthetic films with known (or unknown) structure. This technique will also present new avenues to study the penetration of virus or drug delivery cargo through mucus or mucin

hydrogels,[41, 42] interpreting the microscopic view of particle dynamics during gel electrophoresis or column chromatography,[12, 43] exploring the mechanism behind critical material chemistry, such as self-healing and catalytic processes,[44, 45] and illustrating the dynamics within biomolecular condensates[46].

METHODS

Sample preparation

Agarose powder (type I low EEO, Sigma-Aldrich) was mixed with 1× Tris-Acetate-EDTA buffer (Apex Bioresearch Products, 18-134L) in a microwaveable flask and microwaved until the agarose was completely dissolved without overboiling. Cool down the agarose solution down to about 60 °C in water bath. 100 nm, 200 nm, or 500 nm carboxyl-functionalized polystyrene microspheres (Bangs Laboratories, Inc., FCDG002, FCDG003, or FCDG005) were pre-diluted in distilled water and pre-warmed to about 60 °C in water bath. The anionic carboxyl group on the emitter beads would be expected to have minimal interaction with the anionic agarose.[47] Also, it was demonstrated that premixing probes with agarose gel has no significant impact in gel formation.[27] Equal volume of agarose solution and microsphere dilution were quickly mixed to achieve the desired final concentration. 300 μL of mixture was transferred into a chambered coverslip (Ibidi, 80826). The sample was solidified under room temperature for about 15 minutes and 100 μL distilled water was applied on the top of gel to prevent dehydration.

Validating the tracking of an individual particle

As part of the 3D-SMART mechanism, the EOD continuously scans the particle in a 5×5 grid. The result is a real-time "EOD image" which can be used to evaluate tracking performance. If only one individual particle is being tracked, the center pixel of the EOD image will have most photon counts. If more than one particle exists in the scanning plane, multiple photon-count maxima will exist in a single EOD image, which is also accompanied by an increase in the average particle intensity. These two factors can be used to rule out trajectories containing multiple particles. An example of the system tracking more than one particle is shown in the Supporting Information (fig. S8).

Cavity identification

For 2D cavity identification, trajectories were processed using a sliding window of 180 second window, stepped in 30-second increments. Particle localizations were distributed into 10×10 nm^2 pixels, selected based on the localization precision. The density of localizations in each pixel is convoluted with a 3×3 Gaussian Kernel. Pixels with fewer than 15 localizations were filtered out. Areas were grouped using the `bwconncomp` function in MATLAB. Areas in different segments were merged to form the final result. Areas with fewer than 60 pixels were excluded. This threshold was determined by observing fixed particles.

Similarly, in 3D cavity identification, trajectories were processed using a sliding window algorithm, with 180-second window size and 30-second step size. Particle localizations were distributed into voxels with the size of 10×10×20 nm in XYZ, determined by localization precision. The localization density in each voxel is convoluted with a 3×3×3 Gaussian Kernel. Voxels with fewer than 2 localizations were filtered out. Volumes were grouped using the `bwconncomp` function in MATLAB. Volumes in different segments were merged to form the final result. Final volumes with fewer than 300 voxels were excluded. This lower threshold was determined from trajectories of fixed particles. The volumetric images were plotted with the `vol3d` function.[48]

The pixel/voxel number within each isolated area/volume represents the cavity area/volume size, while numbers of particle localizations within the area/volume represent the dwell time within the area/volume. Measuring uncertainty of the area/volume size is calculated by expanding or shrinking the area/volume by one pixel/voxel.

Position categorization

Positions were categorized based on their spatial relationship to cavities. Positions labeled as 'not-in-cavity' were further classified as follows:

Successful hop: Consecutive positions labeled 'not-in-cavity' that connect two distinct cavities were registered as 'successful hop', indicating pathways or connections between cavities.

Unsuccessful hop: The rest of the consecutive positions labelled 'not-in-cavity' and located within the channel were registered as 'unsuccessful hop', indicating events of particle entering the channel but not successfully pass through.

Measuring uncertainty: All remaining 'not-in-cavity' positions that do not connect cavities are near cavities but lack sufficient sampling to be definitively assigned to any specific cavity. These

positions represent 'measuring uncertainty'. For both thermodynamic and kinetic analysis, these uncertain positions were ignored.

Fractional dwell time equals fractional confinement volume

For diffusing particle constituting isolated states with total volume of V_{tot} and total dwell time of t_{tot}. For each individual state with volume of V_k and dwell time of t_k, according to the partition function, the fractional dwell time is

$$t_k\% \simeq \frac{e^{-F_k/k_BT}}{\sum_i e^{-F_i/k_BT}} \tag{8}$$

in which, F_k the thermodynamic potential energy. In this scenario, the thermodynamic potential is simply contributed by entropy, $F = -ST$, which can be determined using Boltzmann's entropy formula:

$$S = k_B \ln \Omega \tag{9}$$

in which, k_B is Boltzmann's constant, and Ω is the number of microstates within macrostate. Therefore, the fractional time can be written as

$$t_k\% \simeq \frac{e^{S_k/k_B}}{\sum_i e^{S_i/k_B}} = \frac{\Omega_k}{\Omega_{tot}} \tag{10}$$

For the isolated confinements constituted by diffusing particles, Ω is proportional to the volume of confinements, V. Naturally, we have the fractional dwell time equal to the fractional confinement volume.

$$t_k\% \simeq \frac{\Omega_k}{\Omega_{tot}} = \frac{\mathrm{V}_k}{\mathrm{V}_{tot}} = V_k\% \tag{11}$$

AUTHOR INFORMATION

Corresponding Author

Kevin D. Welsher - Department of Chemistry, Duke University; Durham, North Carolina 27708, United States; Email: kdw32@duke.edu

Authors

Yuxin Lin - Department of Chemistry, Duke University; Durham, North Carolina 27708, United States

Haoting Lin - Department of Chemistry, Duke University; Durham, North Carolina 27708, United States

Author Contributions

Y.L. and K.D.W. conceptualized the study. Y.L. and K.D.W. were responsible for the methodology. Y.L. and H.L. performed investigations. K.D.W. was responsible for funding acquisition. Y.L., H.L., and K.D.W. curated the data. Y.L., H.L., and K.D.W. performed the visualization. Y.L. and K.D.W. wrote the original draft and reviewed and edited the manuscript. The manuscript was written through contributions of all authors. All authors have given approval to the final version of the manuscript.

Notes

The authors declare no competing financial interest.

ACKNOWLEDGMENT

We acknowledge financial support from the National Institute of General Medical Sciences of the National Institutes of Health under award number R35GM124868 (K.D.W.). We appreciate the support from the Fitzpatrick Institute for Photonic at Duke University, along with the John T. Chambers Scholarship (to Y.L.). We thank Dr. Michael Rubinstein at Duke University and Dr. Dario Conca at Umeå University for useful discussions. Some schematics were created with BioRender.com.

Reference

(1) Manzo, C.; Garcia-Parajo, M. F. A review of progress in single particle tracking: from methods to biophysical insights. *Rep. Prog. Phys.* **2015**, *78* (12), 124601.
(2) Shen, H.; Tauzin, L. J.; Baiyasi, R.; Wang, W.; Moringo, N.; Shuang, B.; Landes, C. F. Single Particle Tracking: From Theory to Biophysical Applications. *Chem. Rev.* **2017**, *117* (11), 7331-7376. DOI: 10.1021/acs.chemrev.6b00815.

(3) Hou, S.; Johnson, C.; Welsher, K. Real-Time 3D Single Particle Tracking: Towards Active Feedback Single Molecule Spectroscopy in Live Cells. *Molecules* **2019**, *24* (15). DOI: 10.3390/molecules24152826.
(4) Liu, S.-L.; Wang, Z.-G.; Xie, H.-Y.; Liu, A.-A.; Lamb, D. C.; Pang, D.-W. Single-Virus Tracking: From Imaging Methodologies to Virological Applications. *Chem. Rev.* **2020**, *120* (3), 1936-1979. DOI: 10.1021/acs.chemrev.9b00692.
(5) Button, B.; Cai, L.-H.; Ehre, C.; Kesimer, M.; Hill, D. B.; Sheehan, J. K.; Boucher, R. C.; Rubinstein, M. A periciliary brush promotes the lung health by separating the mucus layer from airway epithelia. *Science* **2012**, *337* (6097), 937-941.
(6) Marttin, E.; Schipper, N. G.; Verhoef, J. C.; Merkus, F. W. Nasal mucociliary clearance as a factor in nasal drug delivery. *Advanced drug delivery reviews* **1998**, *29* (1-2), 13-38.
(7) Kisley, L.; Brunetti, R.; Tauzin, L. J.; Shuang, B.; Yi, X.; Kirkeminde, A. W.; Higgins, D. A.; Weiss, S.; Landes, C. F. Characterization of porous materials by fluorescence correlation spectroscopy super-resolution optical fluctuation imaging. *ACS nano* **2015**, *9* (9), 9158-9166.
(8) Ivashchenko, O. Cryo-SEM and confocal LSM studies of agar gel, nanoparticle hydrocolloid, mineral clays and saline solutions. *Scientific Reports* **2022**, *12* (1), 9930.
(9) Maaloum, M.; Pernodet, N.; Tinland, B. Agarose gel structure using atomic force microscopy: gel concentration and ionic strength effects. *Electrophoresis* **1998**, *19* (10), 1606-1610.
(10) Wu, H.; Schwartz, D. K. Nanoparticle tracking to probe transport in porous media. *Acc. Chem. Res.* **2020**, *53* (10), 2130-2139.
(11) von Diezmann, L.; Shechtman, Y.; Moerner, W. E. Three-Dimensional Localization of Single Molecules for Super-Resolution Imaging and Single-Particle Tracking. *Chem Rev* **2017**, *117* (11), 7244-7275. DOI: 10.1021/acs.chemrev.6b00629.
(12) Abe, Y.; Tomioka, N.; Matsuda, Y. Nano-particle motion in monolithic silica column using single-particle tracking method. *Nanoscale Advances* **2024**.
(13) Foreman, K.; Tran-Ba, K.-H. Single-Particle Tracking in Poly (Ethylene Glycol) Diacrylate: Probe Size Effect on the Diffusion Behaviors of Nanoparticles in Unentangled Polymer Solutions. *The Journal of Physical Chemistry B* **2023**, *127* (31), 7091-7102.
(14) Xue, C.; Huang, Y.; Zheng, X.; Hu, G. Hopping behavior mediates the anomalous confined diffusion of nanoparticles in porous hydrogels. *The Journal of Physical Chemistry Letters* **2022**, *13* (45), 10612-10620.
(15) Pavani, S. R. P.; Thompson, M. A.; Biteen, J. S.; Lord, S. J.; Liu, N.; Twieg, R. J.; Piestun, R.; Moerner, W. E. Three-dimensional, single-molecule fluorescence imaging beyond the diffraction limit by using a double-helix point spread function. *Proc. Natl. Acad. Sci. U. S. A.* **2009**, *106* (9), 2995-2999.
(16) Chatterjee, S.; Kramer, S. N.; Wellnitz, B.; Kim, A.; Kisley, L. Spatially resolving size effects on diffusivity in nanoporous extracellular matrix-like materials with fluorescence correlation spectroscopy super-resolution optical fluctuation imaging. *J. Phys. Chem. B* **2023**, *127* (20), 4430-4440.
(17) Yu, D.; Garcia IV, A.; Blum, S. A.; Welsher, K. D. Growth kinetics of single polymer particles in solution via active-feedback 3D tracking. *J. Am. Chem. Soc.* **2022**, *144* (32), 14698-14705.
(18) Tan, X.; Hou, S.; Niver, A.; Zhang, C.; Johnson, A.; Welsher, K. D. Active-feedback 3D single-molecule tracking using a fast-responding galvo scanning mirror. *J. Phys. Chem. A* **2023**, *127* (30), 6320-6328.

(19) Lin, Y.; Exell, J.; Lin, H.; Zhang, C.; Welsher, K. D. Hour-long, kilohertz sampling rate 3D single-virus tracking in live cells enabled by StayGold fluorescent protein fusions. *bioRxiv* **2024**, 2024.2003. 2014.585070.
(20) Johnson, C.; Exell, J.; Lin, Y.; Aguilar, J.; Welsher, K. D. Capturing the start point of the virus–cell interaction with high-speed 3D single-virus tracking. *Nat. Methods* **2022**, *19* (12), 1642-1652. DOI: 10.1038/s41592-022-01672-3.
(21) Van Heerden, B.; Vickers, N. A.; Krüger, T. P.; Andersson, S. B. Real-Time Feedback-Driven Single-Particle Tracking: A Survey and Perspective. *Small* **2022**, *18* (29), 2107024.
(22) Mieskes, F.; Ploetz, E.; Wehnekamp, F.; Rat, V.; Lamb, D. C. Multicolor 3D Orbital Tracking. *Small* **2023**, 2204726.
(23) Bucci, A.; Tortarolo, G.; Held, M. O.; Bega, L.; Perego, E.; Castagnetti, F.; Bozzoni, I.; Slenders, E.; Vicidomini, G. 4D Single-particle tracking with asynchronous read-out single-photon avalanche diode array detector. *Nat. Commun.* **2024**, *15* (1), 6188.
(24) Montiel, D.; Yang, H. Real-time three-dimensional single-particle tracking spectroscopy for complex systems. *Laser & Photonics Reviews* **2010**, *4* (3), 374-385.
(25) Hou, S.; Exell, J.; Welsher, K. Real-time 3D single molecule tracking. *Nat. Commun.* **2020**, *11* (1), 3607. DOI: 10.1038/s41467-020-17444-6.
(26) Balzarotti, F.; Eilers, Y.; Gwosch, K. C.; Gynnå, A. H.; Westphal, V.; Stefani, F. D.; Elf, J.; Hell, S. W. Nanometer resolution imaging and tracking of fluorescent molecules with minimal photon fluxes. *Science* **2017**, *355* (6325), 606-612.
(27) Jayawardena, I.; Turunen, P.; Garms, B. C.; Rowan, A.; Corrie, S.; Grøndahl, L. Evaluation of techniques used for visualisation of hydrogel morphology and determination of pore size distributions. *Materials Advances* **2023**, *4* (2), 669-682.
(28) Hou, S.; Lang, X.; Welsher, K. Robust real-time 3D single-particle tracking using a dynamically moving laser spot. *Opt Lett* **2017**, *42* (12), 2390-2393. DOI: 10.1364/OL.42.002390.
(29) Hou, S.; Welsher, K. An Adaptive Real-Time 3D Single Particle Tracking Method for Monitoring Viral First Contacts. *Small* **2019**, *15* (44), 1903039.
(30) Mermillod-Blondin, A.; McLeod, E.; Arnold, C. B. High-speed varifocal imaging with a tunable acoustic gradient index of refraction lens. *Opt. Lett.* **2008**, *33* (18), 2146-2148.
(31) Fields, A. P.; Cohen, A. E. Optimal tracking of a Brownian particle. *Opt. Express* **2012**, *20* (20), 22585-22601.
(32) Skaug, M. J.; Wang, L.; Ding, Y.; Schwartz, D. K. Hindered nanoparticle diffusion and void accessibility in a three-dimensional porous medium. *ACS nano* **2015**, *9* (2), 2148-2156.
(33) Renner, M.; Wang, L.; Levi, S.; Hennekinne, L.; Triller, A. A simple and powerful analysis of lateral subdiffusion using single particle tracking. *Biophys. J.* **2017**, *113* (11), 2452-2463.
(34) Cai, L.-H.; Panyukov, S.; Rubinstein, M. Hopping diffusion of nanoparticles in polymer matrices. *Macromolecules* **2015**, *48* (3), 847-862.
(35) Wang, D.; Wu, H.; Liu, L.; Chen, J.; Schwartz, D. K. Diffusive escape of a nanoparticle from a porous cavity. *Phys. Rev. Lett.* **2019**, *123* (11), 118002.
(36) Wang, D.; Wu, H.; Schwartz, D. K. Three-dimensional tracking of interfacial hopping diffusion. *Physical Review Letters* **2017**, *119* (26), 268001.
(37) Xue, C.; Shi, X.; Tian, Y.; Zheng, X.; Hu, G. Diffusion of nanoparticles with activated hopping in crowded polymer solutions. *Nano Letters* **2020**, *20* (5), 3895-3904.
(38) Lee, S. V.; Bahaman, A. R. Discriminatory power of agarose gel electrophoresis in DNA fragments analysis. *Gel electrophoresis-principles and basics* **2012**, 41-56.

(39) Kirkpatrick, F. H. Overview of agarose gel properties. In *Current communications in cell & molecular biology*, Vol. 1; Cold Spring Harbor Laboratory Press, 1990; pp 9-22.
(40) Pedone, D.; Langecker, M.; Abstreiter, G.; Rant, U. A pore− cavity− pore device to trap and investigate single nanoparticles and DNA molecules in a femtoliter compartment: confined diffusion and narrow escape. *Nano Lett.* **2011**, *11* (4), 1561-1567.
(41) Joyner, K.; Song, D.; Hawkins, R. F.; Silcott, R. D.; Duncan, G. A. A rational approach to form disulfide linked mucin hydrogels. *Soft Matter* **2019**, *15* (47), 9632-9639.
(42) Kim, J.; Jozic, A.; Lin, Y.; Eygeris, Y.; Bloom, E.; Tan, X.; Acosta, C.; MacDonald, K. D.; Welsher, K. D.; Sahay, G. Engineering Lipid Nanoparticles for Enhanced Intracellular Delivery of mRNA through Inhalation. *ACS Nano* **2022**, *16* (9), 14792-14806.
(43) Johnson, A.; Welsher, K. Single-nanoparticle electrophoretic mobility and trapping using active-feedback 3D tracking. *bioRxiv* **2024**, 2024.2007. 2008.602591.
(44) Iyer, A. S. J.; Lyon, L. A. Self-Healing Colloidal Crystals. *Angew. Chem.* **2009**, *121* (25), 4632-4636.
(45) Dong, B.; Pei, Y.; Zhao, F.; Goh, T. W.; Qi, Z.; Xiao, C.; Chen, K.; Huang, W.; Fang, N. In situ quantitative single-molecule study of dynamic catalytic processes in nanoconfinement. *Nature Catalysis* **2018**, *1* (2), 135-140.
(46) Sundaravadivelu Devarajan, D.; Wang, J.; Szała-Mendyk, B.; Rekhi, S.; Nikoubashman, A.; Kim, Y. C.; Mittal, J. Sequence-dependent material properties of biomolecular condensates and their relation to dilute phase conformations. *Nat. Commun.* **2024**, *15* (1), 1912.
(47) Daniels, C. R.; Kisley, L.; Kim, H.; Chen, W. H.; Poongavanam, M. V.; Reznik, C.; Kourentzi, K.; Willson, R. C.; Landes, C. F. Fluorescence correlation spectroscopy study of protein transport and dynamic interactions with clustered-charge peptide adsorbents. *Journal of Molecular Recognition* **2012**, *25* (8), 435-442.
(48) Woodford, O. *vol3d v2*. MATLAB Central File Exchange, 2025. https://www.mathworks.com/matlabcentral/fileexchange/22940-vol3d-v2 (accessed 2025-02-17).